Polarization insensitivity in square split-ring resonators with asymmetrical arm widths

Qiannan Wu (吴倩男)[1,*], Feng Lan (兰 峰)[1], YaXin Zhang (张雅鑫)[1], HongXin Zeng (曾泓鑫)[1], Ziqiang Yang (杨梓强)[1], and Xi Gao (高 喜)[2]

[1]*School of Physical Electronics, University of Electronic Science and Technology of China, Chengdu 610054, China*
[2]*School of Information and Communication, Guilin University of Electronic Technology, Guilin 541004, China*
**Corresponding author: qiannan28@163.com*

Received May 15, 2015; accepted July 31, 2015; posted online September 17, 2015

A polarization-insensitive, square split-ring resonator (SSRR) is simulated and experimented. By investigating the influence of the asymmetrical arm width in typical SSRRs, we find that the variation of the arm width enables a blue shift of the resonance frequency for the 0° polarized wave and a red shift of the resonance frequency for the 90° polarized wave. Thus, the resonance frequency for the 0° polarized wave and the resonance frequency for the 90° polarized wave will be identical by asymmetrically adjusting the arm width of the SSRR. Two modified, split-ring resonators (MSRRs) that are insensitive to the polarization with asymmetrical arm widths are designed, fabricated, and tested. Excellent agreement between the simulations and experiments for the MSRRs demonstrates the polarization insensitivity with asymmetrical arm widths. This work opens new opportunities for the investigation of polarization-insensitive, split-ring resonator metamaterials and will broaden the applications of split-ring resonators in various terahertz devices.

OCIS codes: 350.2450, 160.3918, 040.2235.
doi: 10.3788/COL201513.101601.

Metamaterials have attracted much attention owing to their unusual electric and magnetic performances, which are not observed in nature[1–4]. They have the potential for applications in terahertz devices, such as converters[5], antennae[6], filters[7–9], and absorbers[10,11]. Split-ring resonators (SRRs) are the most commonly used cells in frequency-selective surface metamaterials because of their classic geometry and resonance characteristics[12–14]. A large number of studies have reported multiple arrangements of SRRs in one-layer[15–17] and multi-layer[16–18] configurations, such as edge-coupled SRRs and broadside-coupled SRRs. A broadband multi-layer terahertz metamaterial was fabricated and tested on flexible substrates with square SRR (SSRRs)[19], and a triple-resonant metamaterial with an asymmetrical, modified SRR (MSRR) single particle in the terahertz band was also designed and measured[20]. What's more, a new coupled mode of two SRRs, which could sustain larger quality factors than those of conventional SRR arrangements, has been designed and measured[21].

With the asymmetrical structure of SRRs, the distinct resonance characteristics of the 0° and 90° polarized waves in SSRRs have been studied[15,18,22]. The SRR polarization-dependent metamaterials have been used to control the effective electric permittivity by tuning the polarized angle of the electric field[23]. But the polarization insensitivity of all polarized angles in asymmetrical, SSRRs has not been achieved so far. In this Letter, the polarization insensitivity of SSRRs with asymmetrical arm widths is presented. Detailed research on two MSRRs is presented. Good agreement between the simulations and the experiments shows that the resonance frequencies of the MSRRs are insensitive to various polarized angles. The polarization-insensitive MSRRs, with their simple structure, would broaden the applications of SRRs in various terahertz devices. Compared to centrosymmetric metamaterials, the polarization-insensitive SRRs with various combination and coupling schemes have the potential for applications in multiband and wideband metamaterials, high gain reflect array metamaterials, high absorption metamaterials, and so on.

The scheme of a classic SSRR unit is illustrated in Fig. 1. The yellow area in Fig. 1 represents the aluminum coating, which consists of arm1 (A_1), arm2 (A_2), and arm3 (A_3). The aluminum film is 0.35 μm thick. The blue area is the quartz substrate with a thickness of 200 μm. The relative permittivity of the quartz layer is $\varepsilon_r = 3.78$. The dimensions for the SSRR unit in Fig. 1 are $P = 240$ μm, $d_0 = 20$ μm, $l = 200$ μm, and $d_1 = d_2 = 20$ μm.

The resonance characteristics for a classic SSRR are determined by utilizing the finite-difference time-domain

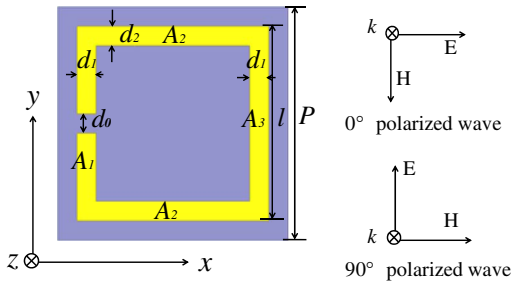

Fig. 1. Classic SSRR structure.

method. In the simulations, a unit cell model is constructed using two floquet ports and a periodic boundary on the four sidewalls. The simulated S_{21} curves from 200 to 600 GHz for a SSRR excited with 0°, 30°, 60°, and 90° polarized waves are given in Fig. 2(a). The difference in the resonance frequencies between the 0° and 90° polarized waves is obvious. The resonance frequency for the 0° polarized wave is $f_0 = 322.8$ GHz. However, there are two resonance frequencies for the 90° polarized wave, f_1 and f_2, located at 140.6 and 410 GHz, respectively. When the polarized angle changed from 0° to 90°, the resonance frequency shift from f_0 to f_2 and f_1 gradually emerged. The resonances at 30° and 60° contributed to two individual orthogonal electric resonances [see Fig. 2(a)][18]. A greater difference between the resonance characteristics for the 0° and 90° polarized waves leads to the SSRR becoming more sensitive to differently polarized orientations. Thus, when the resonance frequencies for the 0° and 90° polarized waves are identical, the resonator will be more polarization insensitive. The SSRR samples are fabricated by photolithography, which uses light to transfer a geometric pattern from a photomask to a light-sensitive chemical photoresist on the substrate. A series of chemical treatments then engraves the exposure pattern into the material underneath the photoresist. The samples are characterized by terahertz-pulsed spectroscopy (TPS-3000, Teraview company) with a frequency resolution of approximately 0.006 THz and a dynamic range of around 80 dB. The terahertz time-domain data, $R(t)$ and $S(t)$, of the reference and sample spectra, respectively, are obtained by averaging the results of repeated measurements. Finally, the frequency-dependent complex transmission coefficient of the sample is determined from $T(\omega) = S(\omega)/R(\omega)$, where $S(\omega)$ and $R(\omega)$ are the time-domain data of the sample and reference spectra, respectively[7]. All the experiments are illuminated by linearly polarized waves. By rotating the array sample in the xy plane, the resonances for differently polarized waves are obtained. Figure 2(b) shows that the experimental results for a SSRR with differently polarized angles agree well with the simulations.

Figure 3 illustrates the influence of d_1 and d_2 on the resonance characteristics for the 0° and 90° polarized waves. In the simulations, both the lengths of the period (P) and

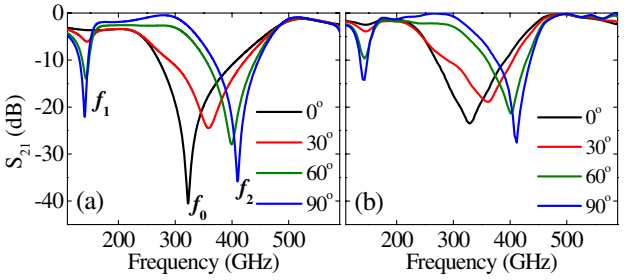

Fig. 2. S_{21} curve for a SSRR with excitations in differently polarized orientations. (a) Simulated results. (b) Experimental results.

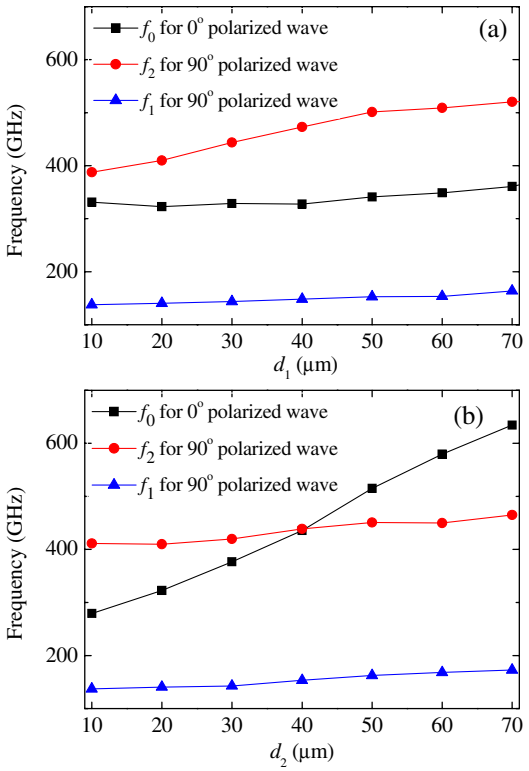

Fig. 3. Influence of d_1 and d_2 on the resonance characteristics for the 0° and 90° polarized waves: (a) with different d_1 values ($d_2 = 20$ μm), (b) with different d_2 values ($d_1 = 20$ μm).

the arms (l) are fixed, while the values of d_1 and d_2 change from 10 to 70 μm. It is obvious that the changes of d_1 and d_2 have little influence on the first resonance for the 90° polarized wave. In Fig. 3(a), with the increase of d_1, the resonance frequency for the 0° polarized wave almost remains unchanged, while for the second resonance of the 90° polarized wave, the frequency increases from 387.6 to 520.2 GHz. Figure 3(b) shows that, with the increase of d_2, the resonance frequency for the 0° polarized wave increases from 279.4 to 634.2 GHz, while for the second resonance of the 90° polarized wave, the frequency only increases from 411.4 to 464.8 GHz. According to the simulation results, d_1 has a larger effect than d_2 on the second resonance for the 90° polarized wave, while d_2 has larger effect than d_1 on the resonance for the 0° polarized wave. In addition, the influence of d_2 on f_0 is much greater than f_2.

The simulated conclusions above could be used to modulate the polarization insensitivity of SSRRs. By choosing suitable values for d_1 and d_2 to synchronize the resonance frequencies of the two modes mentioned above, a method to improve the polarization insensitivity of SSRRs is proposed. As $f_0 = 322.8$ GHz while $f_2 = 410$ GHz in the SSRR with identical arm widths, there is a remarkable blue shift of f_0 by increasing d_2. A red shift of f_2 can be achieved by decreasing d_1.

In order to understand the effects of d_1 and d_2 on the resonances, we investigate the two induced current distributions and paths for the 0° and 90° polarized waves in a

SSRR. The resonance frequency can be obtained using $f = 1/2\pi\sqrt{LC}$. Depending on the LC resonance circuit theory, the equivalent capacitance (C) comes from the interactions between the formed dipoles induced in the SSRRs. The equivalent inductance (L) arises from self-inductance in the arms when currents pass through them[15,24]. The equivalent inductance of the arms increase with the length and decrease with the width[25,26]. C_a, L_a and C_b, L_b are the equivalent capacitances and inductances for the two resonances in Figs. 4(a) and 4(b), respectively. In Fig. 4, the contributions of the equivalent capacitances C_a and C_b to the two resonance modes with the variations of d_1 or d_2 are not strong. According to the LC resonance theory and the results shown in Fig. 3, d_2 has larger effect on L_a than d_1 for the resonance excited with the 0° polarized wave. Thus, the equivalent inductance of A_2 contributes more to L_a of the resonance excited with the 0° polarized wave than A_1 and A_3. In contrast, for the 90° polarized wave, d_1 has larger effect on L_b than d_2, and the equivalent inductance of A_1 and A_3 contributed more to L_a than A_2.

For the 0° polarized wave, the electric field is parallel to arm A_2 and the dipole resonance comes into being on the two arms of A_2. Thus, the energy of the electromagnetic resonance concentrates on A_2. In Fig. 4(a), the average induced current density of A_2 is much stronger than those of A_1 and A_3, while in Fig. 4(b), the average current densities of A_1 and A_3 are slightly stronger than that of A_2. By the comparative analysis above, the average induced current density in the arm is approximately proportional to the relative value of the equivalent inductance in the arm at the LC resonance. Thus, the relative equivalent inductances could not only be determined by the length and width of the equivalent inductance, but also by the average induced current densities in the arms.

Two modified SSRRs with asymmetrical arm widths are designed, fabricated, and tested using terahertz time-domain spectroscopy; they display almost the same resonance frequencies for all polarized angles.

The first MSRR ($MSRR_1$) is fabricated by photolithography, as shown in Fig. 5. The bright part and the dark part of the sample are aluminum film and quartz substrate, respectively. The $MSRR_1$ and simulated S_{21} results

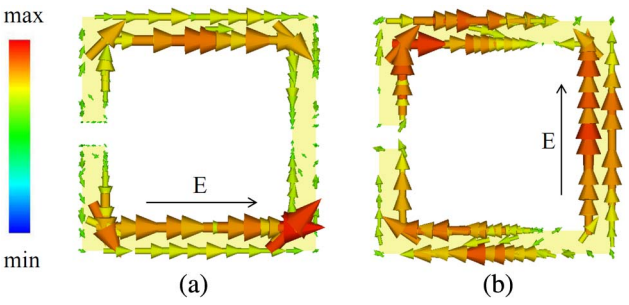

Fig. 4. Surface-induced current distributions of the SSRR (a) for the 0° polarized wave at 322.8 GHz, (b) for the 90° polarized wave at 410 GHz.

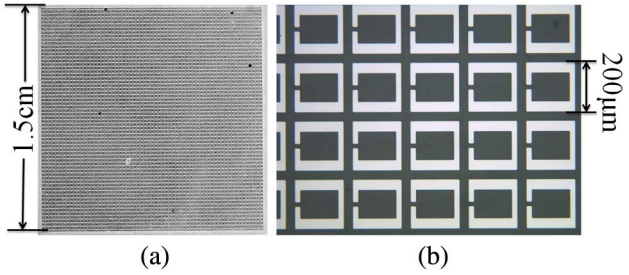

Fig. 5. (a) Photograph and (b) microscope image of $MSRR_1$.

for polarized angles of 0°, 30°, 60°, and 90° are illustrated in Fig. 6(a). The design of $MSRR_1$ corresponds to the crossover point in Fig. 3(b), where d_1 remains at 20 μm and d_2 increases to 40 μm. The simulated resonance dips for the polarized angles of 0°, 30°, 60°, and 90° are −43.6 dB at 436 GHz, −39.7 dB at 435 GHz, −35.6 dB at 436.6 GHz, and −34.4 dB at 438.8 GHz, respectively. In Fig. 6(b), the experimental resonance dips for the polarized angles of 0°, 30°, 60°, and 90° are −33.2 dB at 440 GHz, −29.24 dB at 440 GHz, −26.9 dB at 443.6 GHz, and −25.45 dB at 443 GHz, respectively. By comparing Figs. 2 and 6, one can see that the performance of the resonance of $MSRR_1$ is not sensitive to the polarization angle. The resonance frequencies and losses in the experimental results are greater than those in the simulation results. The larger losses in the experiments are likely caused by small differences in the metal films and substrates used in the fabricated sample and simulation model[27]. In Fig. 6(b), the values of d_1 and d_2 for the fabricated $MSRR_1$ are around 22.4 and 42.6 μm, respectively (measured with a microscope). From the results above, the increments of d_1 and d_2 result in small blue shifts of the resonance frequencies obtained from the experiments shown in Fig. 6 for both the 0° and 90° polarized waves.

All of the simulated and experimental results thus far are for different polarized waves at vertical incident angles (along the z-direction). Figure 7 illustrates the simulated S_{21} of the $MSRR_1$ for the 0° and 90° polarized waves, when the incident angles are 15° and 30°. It shows that both the resonance frequencies for the 0° and 90° polarized waves have a slightly red shift when the incident angle changes from 0° to 30°. The resonance dips are all under −30 dB.

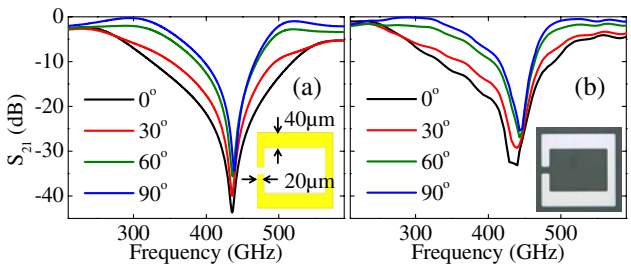

Fig. 6. S_{21} for $MSRR_1$ excited with differently orientated linearly polarized waves. (a) Simulations. (b) Experiments.

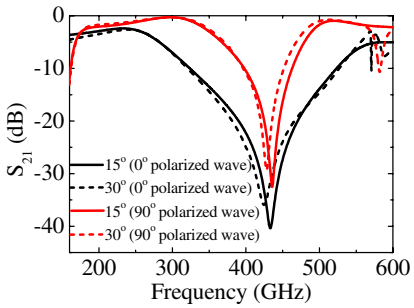

Fig. 7. Simulated S_{21} of $MSRR_1$ for the 0° and 90° polarized waves with 15° and 30° incident angles.

Thus, the modified SRR operates quite well up to an incident angle of 30°.

There are many combinations of d_1 and d_2 with polarization insensitivities for the 0° and 90° polarized waves, based on the abovementioned method. Figure 8 shows a photograph and a microscope image of $MSRR_2$, where the array size of the sample is set to 1.5 cm^2 with 62 × 62 unit cells. $MSRR_2$ was designed with a narrow conductive strip width for low losses. In the design of the $MSRR_2$, d_1 is decreased to 10 μm, which reduces the resonance frequency for the 90° polarized wave, while d_2 is increased to 35 μm, which raises the resonance frequency for the 0° polarized wave. Finally, both the resonance frequencies of the 0° and 90° polarized waves are around 403.1 GHz. As shown in Fig. 9(a), the simulated resonance dips with the polarized angles of 0°, 45°, and 90° are −42.3 dB at 407 GHz, −35.7 dB at 406.8 GHz, and −31.3 dB at 401.2 GHz, respectively. Figure 9(b) shows the experimental results for $MSRR_2$ at the polarized angles of 0°, 45°, and 90°, where the resonance dips are −38.9 dB at 415 GHz, −30.5 dB at 418 GHz, and −28.9 dB at 422 GHz, respectively. The slight difference in the resonance frequencies between the experiments and simulations is caused by machining errors, where the d_1 and d_2 values for the fabricated $MSRR_2$ are 11.1 and 36.6 μm, respectively. Increasing the inductive strip widths leads to blue shifts for the resonances excited by the 0° and 90° polarized waves. The analysis for the two MSRRs illustrates that the experimental results agree well with the simulation results. Furthermore, the two MSRRs could both modulate the resonance bandwidth by controlling the polarized angle.

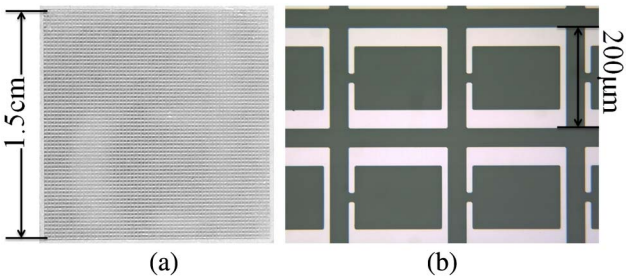

Fig. 8. (a) Photograph and (b) microscope image of $MSRR_2$.

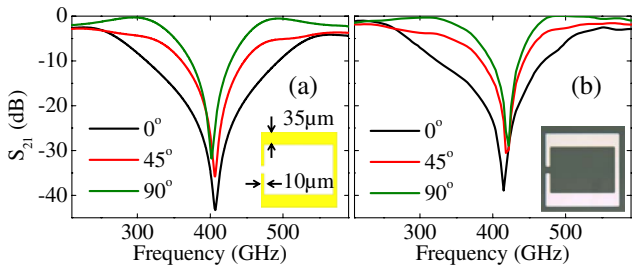

Fig. 9. S_{21} for $MSRR_2$ excited with differently orientated linearly polarized waves. (a) Simulations (b) Experiments.

In conclusion, by analyzing the surface-induced current distribution and paths in a typical SSRR, adjusting the arm width has remarkable influence on the resonance frequencies for differently polarized waves. For the 0° polarized wave, increasing the arm width d_2 achieves a blue shift of the resonance frequency, while for the 90° polarized wave, decreasing the arm width d_1 leads to a red shift of the resonance frequency. According to the results, two polarization-insensitive MSRRs with asymmetrical arm widths are designed, fabricated, and tested. The experimental results agree well with the simulations and attest to the polarization insensitivity of the MSRRs with asymmetrical arm widths. The research results can be utilized for designing polarization-insensitive terahertz metamaterials, and the polarization-insensitive MSRRs with simple structures have extensive potential applications in enhanced-performance metamaterials devices.

This work was supported by the National High Technology Research and Development Program of China (No. 2011AA010204), the National Natural Science Foundation of China (Nos. 91438118 and 61370011), and the Fundamental Research Funds for the Central Universities of China (No. ZYGX2014J037).

References

1. R. A. Shelby, D. R. Smith, and S. Shultz, Science **292**, 77 (2001).
2. H. Chen, W. J. Padilla, J. M. O. Zide, A. C. Gossard, A. J. Taylor, and R. D. Averitt, Nature **444**, 597 (2006).
3. F. Zhang, Q. Zhao, J. Zhou, and S. Wang, Opt. Express **21**, 19675 (2013).
4. Y. Liu, Y. Cheng, Y. Gao, S. Li, and C. Fang, Optik **125**, 2129 (2014).
5. N. K. Grady, J. E. Heyes, D. R. Chowdhury, Y. Zeng, M. T. Reiten, A. K. Azad, A. J. Taylor, D. A. R. Dalvit, and H.-T. Chen, Science **340**, 1304 (2013).
6. M. Huang, Y. Zhou, and T. Chen, Chin. Phys. Lett. **27**, 014102 (2010).
7. F. Lan, Z. Yang, L. Qi, X. Gao, and Z. Shi, Opt. Lett. **39**, 1709 (2014).
8. Y. Z. Cheng, W. Withayachumnankul, A. Upadhyay, D. Headland, Y. Nie, R. Z. Gong, M. Bhaskaran, S. Sriram, and D. Abbott, Appl. Phys. Lett. **105**, 181111 (2014).
9. Y. Ding, G. Zhang, and Y. Cheng, Phys. Scr. **85**, 065405 (2012).
10. J. Han, Z. Tian, J. Gu, M. He, and W. Zhang, Chin. Opt. Lett. **9**, S10401 (2011).

11. B. Na, J. Shi, C. Guan, and Z. Wang, Chin. Opt. Lett. **11**, 111602 (2013).
12. F. Zhang, Q. Zhao, Y. Liu, C. Luo, and X. Zhao, Chin. Phys. Lett. **21**, 1330 (2004).
13. H. Luo, T. Wang, R. Gong, Y. Nie, and X. Wang, Chin. Phys. Lett. **28**, 034204 (2011).
14. F. Zhang, Q. Zhao, J. Sun, J. Zhou, and D. Lippens, Prog. Electromagnet. Res. **124**, 233 (2012).
15. D. R. Chowdhury, R. Singh, A. J. Taylor, H.-T. Chen, W. Zhang, and A. K. Azad, Int. J. Opt. **2012**, 148985 (2012).
16. R. Marqués, F. Medina, and R. Rafii-El-Idrissi, Phys. Rev. B **65**, 144440 (2002).
17. R. Marqués, F. Mesa, J. Martel, and F. Medina, IEEE Trans. Antennas Propag. **51**, 2572 (2003).
18. M. Mutlu, A. E. Akosman, A. E. Serebryannikov, and E. Ozbay, Phys. Rev. Lett. **108**, 213905 (2012).
19. N. R. Han, Z. C. Chen, C. S. Lim, B. Ng, and M. H. Hong, Opt. Express **19**, 6990 (2011).
20. Y.-X. Zhang, S. Qiao, W.-X. Huang, W. Ling, L. Li, and S.-G. Liu, Appl. Phys. Lett. **99**, 073111 (2011).
21. I. Al-Naib, E. Hebestreit, C. Rockstuhl, F. Lederer, D. Christodoulides, T. Ozaki, and R. Morandotti, Phys. Rev. Lett. **112**, 183903 (2014).
22. F. Zhang, Z. Liu, K. Qiu, W. Zhang, C. Wu, and S. Feng, Appl. Phys. Lett. **106**, 061906 (2015).
23. C.-Y. Chen and T.-J. Yen, J. Phys. D: Appl. Phys. **42**, 185402 (2009).
24. D. S. Wilbert, M. P. Hokmabadi, P. Kung, and S. M. Kim, IEEE Trans. Terahertz sci. Technol. **3**, 846 (2013).
25. H.-T. Chen, H. Yang, R. Singh, J. F. O'Hara, A. K. Azad, S. A. Trugman, Q. X. Jia, and A. J. Taylor, Phys. Rev. Lett. **105**, 247402 (2010).
26. F. E. Terman, *Radio Engineers' Handbook* (McGraw-Hill, New York, 1943).
27. L. Huang, D. R. Chowdhuy, S. Ramani, M. T. Reiten, S.-N. Luo, A. K. Azad, A. J. Taylor, and H. T. Chen, Appl. Phys. Lett. **101**, 101102 (2012).